Research
Medical Engineering—Article

SWIR Fluorescence Imaging *In Vivo* Monitoring and Evaluating Implanted M2 Macrophages in Skeletal Muscle Regeneration

Mo Chen [a,b,#], Yuzhou Chen [a,#], Sijia Feng [a,#], Shixian Dong [c], Luyi Sun [a], Huizhu Li [a], Fuchun Chen [d], Nguyen Thi Kim Thanh [e,f], Yunxia Li [a], Shiyi Chen [a], You Wang [b,*], Jun Chen [a,*]

[a] Sports Medicine Institute of Fudan University, Department of Sports Medicine, Huashan Hospital, Fudan University, Shanghai 200040, China
[b] Department of Bone and Joint Surgery, Department of Orthopedics, Renji Hospital, School of Medicine, Shanghai Jiaotong University, Shanghai 200127, China
[c] Department of Anatomy and Physiology, School of Medicine, Shanghai Jiao Tong University, Shanghai 200025, China
[d] Key Laboratory of Infrared System Detection & Imaging Technology, Shanghai Institute of Technical Physics, Chinese Academy of Sciences, Shanghai 200083, China
[e] Biophysics Group, Department of Physics and Astronomy, University College London, London WC1E 6BT, UK
[f] Healthcare Biomagnetics and Nanomaterials Laboratories, University College London, London W1S 4BS, UK

ARTICLE INFO

ABSTRACT

Skeletal muscle has a robust regeneration ability that is impaired by severe injury, disease, and aging, resulting in a decline in skeletal muscle function. Therefore, improving skeletal muscle regeneration is a key challenge in treating skeletal muscle-related disorders. Owing to their significant role in tissue regeneration, implantation of M2 macrophages (M2Mø) has great potential for improving skeletal muscle regeneration. Here, we present a short-wave infrared (SWIR) fluorescence imaging technique to obtain more *in vivo* information for an in-depth evaluation of the skeletal muscle regeneration effect after M2Mø transplantation. SWIR fluorescence imaging was employed to track implanted M2Mø in the injured skeletal muscle of mouse models. It is found that the implanted M2Mø accumulated at the injury site for two weeks. Then, SWIR fluorescence imaging of blood vessels showed that M2Mø implantation could improve the relative perfusion ratio on day 5 (1.09 ± 0.09 vs 0.85 ± 0.05; $p = 0.01$) and day 9 (1.38 ± 0.16 vs 0.95 ± 0.03; $p = 0.01$) post-injury, as well as augment the degree of skeletal muscle regeneration on day 13 post-injury. Finally, multiple linear regression analyses determined that post-injury time and relative perfusion ratio could be used as predictive indicators to evaluate skeletal muscle regeneration. These results provide more *in vivo* details about M2Mø in skeletal muscle regeneration and confirm that M2Mø could promote angiogenesis and improve the degree of skeletal muscle repair, which will guide the research and development of M2Mø implantation to improve skeletal muscle regeneration.

1. Introduction

The skeletal muscle is the most abundant tissue in the human body, with more than 600 pieces accounting for nearly half of the body weight [1–3]. As an important part of the motor system, skeletal muscle participates in various mechanical activities such as maintaining posture, movement, and breathing [3,4]. Although skeletal muscle has robust regeneration ability and can achieve full functional and structural recovery from mild injury, severe injury and other related diseases can impair regeneration ability, leading to decreased motor function and a series of complications. These disorders that impair the regenerative ability of skeletal muscle are mainly divided into the following three categories. ① Injury: As the most common sports injury, skeletal muscle injury accounts for approximately 50% of all sports injuries [5] and is often accompanied by scarring and other poor healing problems manifested by delayed functional recovery, recurrence, chronic pain, and even amputation [6,7]. ② Inflammation: Idiopathic inflammatory myopathies (IIMs) are a heterogeneous group of muscular autoimmune diseases characterized by skeletal muscle inflammation, including dermatomyositis, polymyositis, inclusion body myositis, and other specific types of idiopathic myositis [8]. Mild clinical manifestations include chronic weakness, fatigue, muscle pain, and tenderness, whereas patients with severe symptoms cannot complete basic activities such as dressing, walking, and sitting [9,10].

---

 * Corresponding authors.
   E-mail addresses: drwangyou@126.com (Y. Wang), biochenjun@fudan.edu.cn (J. Chen).
 # These authors contributed equally to this work.

③ Aging: Skeletal muscle aging, also known as sarcopenia, is characterized by a decreased number, strength, and regenerative ability of the skeletal muscle [11,12]. Sarcopenia increases the risk of falls, fractures, cognitive decline, and cardiovascular disease and is associated with increased mortality [13]. A common and core issue in the treatment of all skeletal muscle disorders is improving skeletal muscle regeneration [14–16], which is presently both an opportunity and a challenge.

Macrophages are present in all tissues and have diverse functional subtypes. They are involved in the development, homeostasis, immune processes, and tissue repair [17] and are considered one of the primary regulators of skeletal muscle regeneration [18,19]. In particular, M2 macrophages (M2Mø) are crucial in the late stage of regeneration [2]. A large body of evidence suggests that M2Mø can positively promote regeneration by promoting myocyte regeneration and improving angiogenesis [20,21]. Moreover, M2Mø belong to the non-proliferative cell group and can live for two to three weeks under suitable conditions, which are safer after implantation. In conclusion, these characteristics of M2Mø make it a great candidate with development potential in cell therapy to improve the repair quality of skeletal muscle disorders. However, the *in vivo* efficacy of M2Mø transplanted into repaired skeletal muscle remains to be investigated due to the lack of an effective *in vivo* imaging technique to monitor the relevant dynamic changes after M2Mø implantation in skeletal muscle regeneration.

Short-wave infrared (SWIR) fluorescence imaging is an emerging *in vivo* imaging technique studied since the beginning of the 21st century [22,23]. Compared with conventional optical imaging technology, SWIR fluorescence imaging has outstanding advantages, including real-time capability, high spatial resolution, and deep penetration. Therefore, this technology has developed rapidly in less than two decades, showing great potential in living cell fluorescence tracing systems and vascular imaging at the living level. In our preliminary study, quantum dots (QDs) were prepared as SWIR fluorescent nanoprobes to label bone marrow mesenchymal stem cells (BMSCs) and track the *in vivo* fate of BMSCs injected into a rotator cuff tear model [24]. QDs have also been injected through the tail vein of mice to monitor the growth distribution of neovascularization in injured skeletal muscle in both the temporal and spatial dimensions [25]. All results confirmed the success of this technique in the field of *in vivo* imaging of cells and blood vessels. This work used the technology in the above two aspects of the application (Fig. 1). M2Mø were first labeled with QDs to monitor the aggregation site and residence time of M2Mø after implantation into injured skeletal muscle. Then, SWIR fluorescence imaging was used to monitor blood vessels in injured skeletal muscle *in vivo* to assess the degree of skeletal muscle regeneration. This method was used to compare the M2Mø implantation group and the control group, supplemented by pathological staining and other *in vitro* detection of neovascularization, which proved that compared with the control group, M2Mø implantation group significantly increased neovascularization and improved the degree of skeletal muscle regeneration. In a word, this work will provide more *in vivo* data for M2Mø therapy and guide the development of M2Mø implantation to improve skeletal muscle regeneration.

2. Methods

2.1. Extraction and polarization of mouse bone-marrow-derived macrophages (BMDMs)

The method of extraction and polarization of BMDMs was modified from that described in Ref. [26]. Bone marrow was isolated from the femurs and tibia of Institute of Cancer Research (ICR)
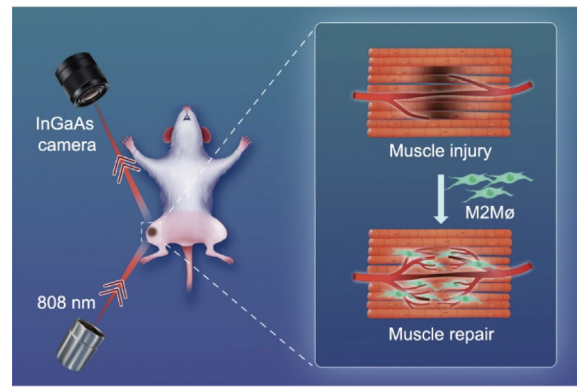

Fig. 1. M2Mø fate and neovascularization after M2Mø implantation in injured skeletal muscle under SWIR fluorescence imaging.

female mice of 6–8 weeks. Cells were differentiated into BMDMs by culturing in Roswell Park Memorial Institute (RPMI)-1640 medium (Servicebio, China) added 10% fetal bovine serum (FBS), 1% penicillin and streptomycin solution (100×; HyClone, USA), and 1% sodium pyruvate (HyClone) by volume. Cells were added to a Petri dish, and then granulocyte–macrophage colony-stimulating factor (GM-CSF; PeproTech, USA) was added at 20 ng·mL^{-1} and placed in a cell incubator (37 °C, 5% CO$_2$, saturated humidity) for culture. Half of the volume and all of the culture medium in each Petri dish were replaced on days 2 and 3, and the new culture medium was supplemented with GM-CSF at 40 and 20 ng·mL^{-1}. On day 6, all culture media in each Petri dish were replaced. The cells in the Petri dishes were bone marrow-derived macrophages (M0 type), and their morphology was observed under a microscope and photographed. Interleukin 4 (IL-4) (10 ng·mL^{-1}) was then added to the fresh medium. On day 8, M2Mø were obtained, and their morphology was observed under a microscope and photographed.

2.2. Quantitative real-time polymerase chain reaction (qRT-PCR)

After M2Mø were rinsed with ice-cold phosphate-buffered saline (PBS), 1 mL RNA Extraction was added to each 3.5 cm diameter Petri dish to directly dissolve the cells. Total RNA was extracted and reverse-transcribed into complementary DNA (cDNA) by adding the following reagents into a sterile, nuclease-free tube on ice in the indicated order: template RNA 2 μg, Primer Oligo (dT) 18 primer 0.5 μL and Random Hexamer primer 0.5 μL or gene-specific primer 1 μL, 5 × Reaction Buffer 4 μL, Servicebio®RT Enzyme Mixa 1 μL, and water nuclease-free to 20 μL. The primer information is shown in Table S1 in Appnedix A. For each 15-μL reaction, prepare the following reaction mix 7.5 μL: F/R primers (2.5 μmol·L^{-1}) 1.5 μL, cDNA 2.0 μL, water nuclease-free 4.0 μL. After PCR amplification, gene expression was normalized to glyceraldehyde-3-phosphate dehydrogenase (GAPDH), which was used as a housekeeping gene. The messenger RNA (mRNA) abundance was quantified using the threshold cycle values by the $2^{-\Delta\Delta c_t}$ comparative method.

2.3. Flow cytometry

Cluster of differentiation 11b (CD11b) and F4/80: The suspension of the polarized M2Mø on day 8 after culture was added into the flow tube to ensure that the number of cells per tube was more than 1×10^6. The supernatant was discarded after centrifugation at 1500 revolutions per minute (rpm) for 5 min. The precipitation was mixed with 50 μL of diluted primary antibody (CD11b and

F4/80), and 2 mL PBS was added after incubation at 4 °C for 30 min in the dark to terminate the reaction. After centrifugation at 1500 rpm for 5 min, the supernatant was discarded, and the precipitate was resuspended in 1× PBS and tested on the machine.

CD206: 100 μL intracellular (IC) fixation buffer was added to the cell precipitate and kept in the dark for 45 min. Add 2 mL 1× perm buffer, centrifuge 1500 rpm for 5 min, and remove supernatant. Next, 100 μL 1× perm buffer was used to suspend the cells, intracellular antibody CD206 was added, and the cells were incubated for 30 min in the dark. Add 2 mL 1× perm buffer, centrifuge 1500 rpm for 5 min, and remove supernatant. The cells were suspended with 500 μL staining buffer and tested on the machine.

2.4. Preparation of M2Mø labeled with QDs

The method for preparing QDs has been described previously [25]. Briefly, 500 μL of 50 mg·mL^{-1} ribonuclease-A from bovine pancreas (Sigma-Aldrich, USA) was mixed with 500 μL of 10 mmol·L^{-1} lead (II) acetate trihydrate, then 50 μL of 1 mol·L^{-1} NaOH solution and 50 μL of 10 mmol·L^{-1} Na$_2$S aqueous solution was added in sequence. The mixture was reacted at 70 °C for 30 s in a microwave reactor (Discover SP; CEM, USA) with an input power of 30 W. The as-prepared QDs were dialyzed three times to remove excess reagents and neutralized. The prepared QDs have an emission peak of around 1300 nm, fluorescent quantum yield (Φf) of 17.3, and an average size of (4.35 ± 0.07) nm [27].

Add 1 mL 0.1 mol·L^{-1} 2-(N-morpholino)ethanesulfonic acid (MES) solution to 0.5 mL QDs solution to adjust the system pH to 5.5–6.5, add 2.4 mg 1-ethyl-3-(3-dimethylaminopropyl) carbodiimide hydrochloride (EDC) and 2.4 mg N-hydroxysuccinimide (NHS), and stir for 20–40 min. Add 1 mg sulfo-smcc dissolved in dimethyl sulfoxide (DMSO) to the system, stir for 2 h, and add 1 mg trans-activator of transcription (TAT) peptide overnight at 4 °C. Transfer to 10 kilodalton (kDa) ultrafiltration tube, centrifuge to 0.5 mL. Add 2.0 × 10^5 M2Mø, co-incubated for 2–4 h, then centrifuge at 1200 rpm for 5 min, discard the supernatant, resuspend in 1× PBS, and repeat three times to wash the unreacted QDs in the system. Finally, the precipitation was suspended to a volume of 100 μL (2.0 × 10^5) M2Mø with 1× PBS.

2.5. Model

All experimental animals were 6–8 weeks ICR female mice provided by Shanghai Jie Si Jie Laboratory Animal Co. Ltd. (China). The study protocol was approved by the Institutional Animal Care and Use Committee of the Medicine School of Fudan University.

The establishment of the cardiotoxin (CTX)-induced skeletal muscle injury mouse model was based on published methods in Ref. [28]. A dose of 120 μL CTX solution (10 μmol·L^{-1}) was injected into the gastrocnemius, soleus, and tibialis anterior muscles. After the mice were euthanized, hind limb skin was exposed to observe skeletal muscle necrosis.

2.6. SWIR fluorescence imaging

The *in vitro* imaging of M2Mø labeled with QDs was performed using a SWIR fluorescence microscopic imaging instrument developed by the Shanghai Institute of Materia Medica, Chinese Academy of Sciences. Before each *in vivo* imaging, the mice (n = 3 per time point) were fixed in the supine position with the lower abdomen and hind limbs depilated after anesthesia. The excitation light source was an 808 nm diode laser. The light emitted from the mice was filtered using a 1250 nm long-pass filter and collected using a two dimensional (2D) InGaAs camera (Photonic Science, UK) at exposure times of 50–100 ms for SWIR fluorescence imaging.

2.6.1. Tracking the fate of implanted M2Mø in vivo using SWIR fluorescence imaging

We injected 100 μL cell suspension of M2Mø labeled with QDs (2.0 × 10^5 M2Mø) into the injured area of the mouse hindlimb on day 3 post-injury. Subsequently, SWIR fluorescence imaging of the injured hind limb was performed on days 3, 9, 15, and 17 post-injury.

2.6.2. Monitoring the blood vessels in skeletal muscle using SWIR fluorescence imaging

QDs (0.3 mL) were injected intravenously before the SWIR fluorescence imaging of blood vessels in the skeletal muscle. Before M2Mø implantation, normal and injured hindlimb muscles were imaged on days 1 and 3 post-injury. After M2Mø implantation, the injured hindlimb muscle was imaged on days 5, 9, and 13 post-injury.

2.7. Analysis of SWIR fluorescence imaging results

The fluorescence intensity (FL) was measured using the ImageJ software. The total value of FL was calculated as the integrated density using ImageJ software. The normalized mean and total values of FL on days 9, 15, and 17 post-injury were normalized for the value on day 3 post-injury.

The signal-to-noise ratio (SNR) was calculated in the same way as Ref. [25], and Eq. (1) can be expressed as

$$\mathrm{SNR} = \frac{\mathrm{FL(S)}}{\sigma} \qquad (1)$$

where FL(S) represents the mean FL corresponding to the sample of QDs, and σ represents the standard deviation of FL of the background without the sample.

Calculation of the relative perfusion ratio was based on the method described by Ma et al. [29], and Eq. (2) can be expressed as

$$\mathrm{Relative\ perfusion\ ratio} = \frac{\mathrm{FL\ of\ CTX\ injection\ area}}{\mathrm{FL\ of\ control\ area}} \qquad (2)$$

The relative perfusion growth rate was used to reflect the rate of new blood vessel growth in the skeletal muscle, as shown in Eq. (3) can be expressed as

$$\mathrm{Relative\ perfusion\ growth\ rate} = \frac{\Delta \mathrm{Relative\ perfusion\ ratio}}{\Delta \mathrm{Time}} \qquad (3)$$

where ΔRelative perfusion ratio represents the difference value of relative perfusion ratio between this time point and the last time point, and ΔTime represents the difference in days between this time point and the last.

2.8. Immunohistochemistry and quantitative analysis

The following primary antibodies and dilution multiples were used for immunohistochemistry: CD163 (Ab182422, 1:500; Abcam, UK), platelet endothelial cell adhesion molecule-1 (CD31; Ab182981, 1:2000; Abcam), α-smooth muscle actin (α-SMA; 14395–1-AP, 1:3000; Proteintech, China), and von Willebrand factor (VWF; 11778–1-AP, 1:250; Proteintech). The skeletal muscle tissue was placed in 4% paraformaldehyde before routine paraffin embedding. First, 4-μm cross-sections were deparaffinized and rehydrated. Then they were immersed in sodium citrate antigen retrieval solution, blocked in 3% H$_2$O$_2$, covered with 10% normal rabbit serum at room temperature for 30 min, incubated overnight with rabbit anti-CD31 antibody (ab182981, 1:1,000; Abcam), followed by secondary antibody horseradish peroxidase (HRP)-conjugated goat anti-rabbit immunoglobulin G (IgG; GB23303, 1:200; Servicebio). Immunohistochemical (IHC) quantification was performed for each high-power field

(magnification 200×). The IHC H-scores were calculated as reported [30].

2.9. Statistical analysis

Values for measurements are expressed as mean ± standard deviation (SD). The significance between the two groups was analyzed using a two-tailed Student's *t*-test. Statistical analyses, including Pearson's correlation matrix and multiple linear regression analyses, were performed using GraphPad Prism 8. $p < 0.05$ was considered at $p < 0.01$ to be highly statistically significant.

3. Results

3.1. In vitro *polarization and SWIR fluorescence labeling of M2Mø*

M2Mø were extracted and polarized from BMDMs and were labeled with SWIR QDs *in vitro* to prepare for subsequent intramuscular implantation and *in vivo* SWIR fluorescence tracing. Cell morphology significantly changed on day 8 of culture compared with that before the addition of IL-4 on day 6 of culture, which preliminarily suggested that macrophages were polarized to M2Mø (Fig. 2(a)). The results of flow cytometry and qRT-PCR further confirmed the success of M2Mø polarization. Furthermore, flow cytometry results showed that 98.74% of M2Mø on day 8 of culture
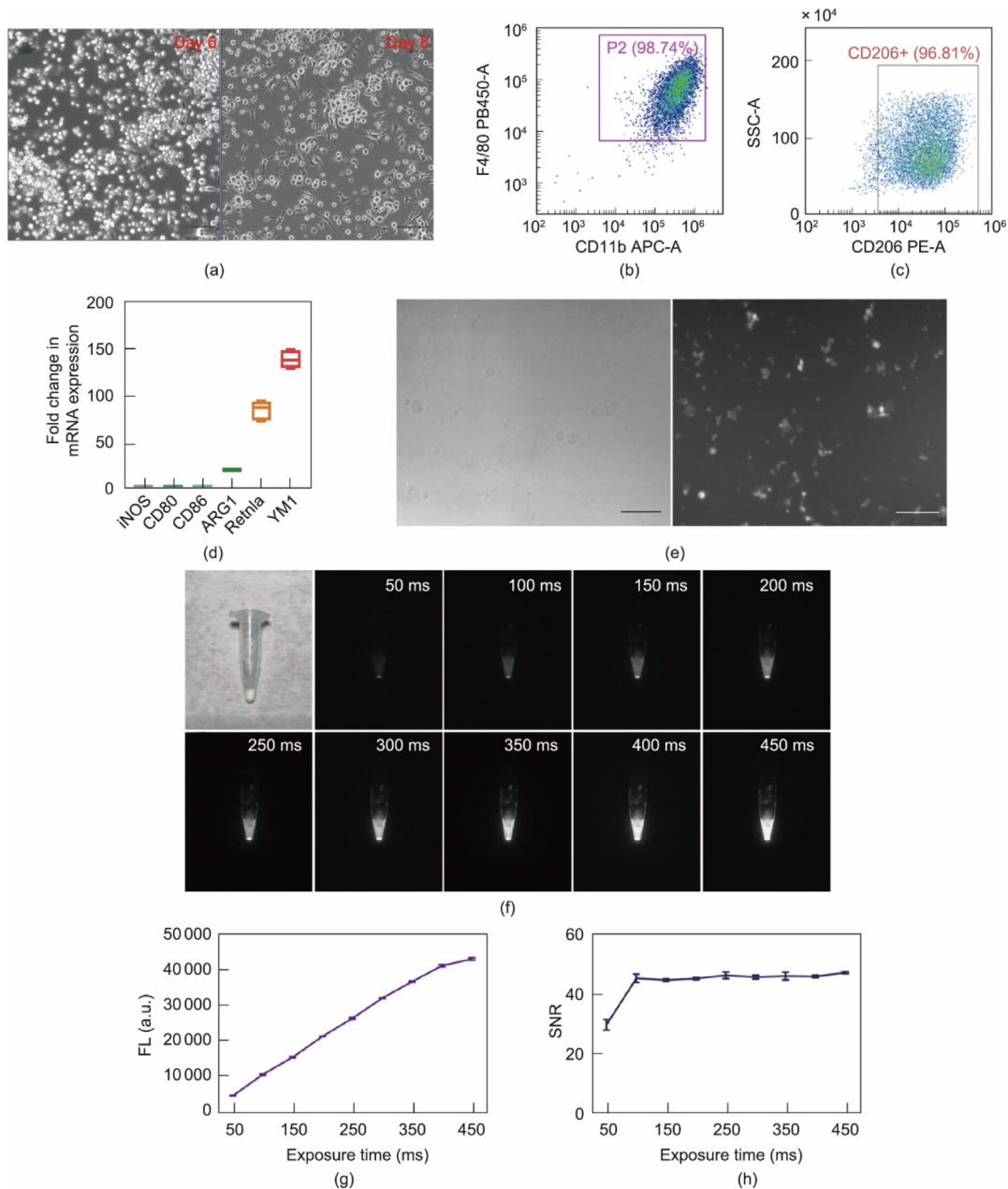

Fig. 2. Polarization of M2Mø and SWIR fluorescence performance of M2Mø labeled with QDs *in vitro*. (a) Unpolarized macrophages on day 6 of culture and the polarized M2Mø on day 8 of culture in the 100× magnification microscope field (scale bar, 100 μm). Results of flow cytometry staining for (b) F4/80 and CD11b antibody, and for (c) CD206 antibody in polarized M2Mø on day 8 of culture. (d) The qRT-PCR expression level of iNOS, CD80, CD86, ARG1, retnla, and YM1 in the polarized M2Mø on day 8 of culture. (e) Labeled M2Mø diluted with PBS solution in Petri dishes under visible light and SWIR microscope (20× magnification), respectively (scale bar, 50 μm). (f) Labeled M2Mø in a 1.5 mL centrifuge tube under visible light and SWIR fluorescence at exposure times of 50–450 ms. (g) FL and (h) SNR of labeled M2Mø at exposure times of 50–450 ms, respectively. P2: F4/80 + CD11b+; PB450-A: pacific blue 450-A; APC-A: allophycocyanin-A; SSC-A: side scatter-A; PE-A: phycoerythrin-A; a.u.: absorbance unit.

were positive for F4/80 and CD11b (Fig. 2(b)), and 96.81% were positive for CD206 (Fig. 2(c)). Meanwhile, the results of qRT-PCR showed that compared to the M1Mø markers such as inducible nitric oxide synthase (iNOS; < 1-fold), CD80 (< 1-fold), and CD86 (< 1-fold), the expression level of M2Mø markers such as arginase 1 (ARG1; 19-fold), retnla (84-fold), and chitinase 3-like 3 (YM1; 137-fold) was exponentially higher (Fig. 2(d)). After confirming polarization, M2Mø were labeled with SWIR QDs for SWIR fluorescence imaging. The SWIR fluorescence profile of the labeled M2Mø was consistent with that observed under visible light in the same field at 20× magnification (Fig. 2(e)), indicating that M2Mø were successfully labeled by SWIR fluorescence. In addition, as shown in Fig. 2(f), the labeled M2Mø were white precipitates in PBS solution under visible light. They showed strong SWIR fluorescence signals at an 808 nm excitation laser. In addition, the FL gradually increased with an increase in exposure time from 50 to 450 ms

(Fig. 2(g)). In contrast, the SNR first increased and then remained relatively stable when the exposure time exceeded 100 ms (Fig. 2(h)). These results indicated that M2Mø were successfully isolated, polarized, and then labeled by SWIR QDs, suggesting labeled M2Mø ready for following SWIR fluorescence imaging.

3.2. Implanted M2Mø accumulated in the injured area for 14 days

Then, the polarized M2Mø were implanted into the injured skeletal muscle on day 3 post-injury (Fig. 3(a)). Compared with the white necrotic tissue observed in the control group without M2Mø transplantation, the area of necrotic tissue in the skeletal muscle after M2Mø transplantation was significantly reduced (Fig. 3(b)). This result suggested that skeletal muscle repair could be improved after M2Mø implantation. As shown in Fig. 3(c), extensive fluorescence was observed immediately after
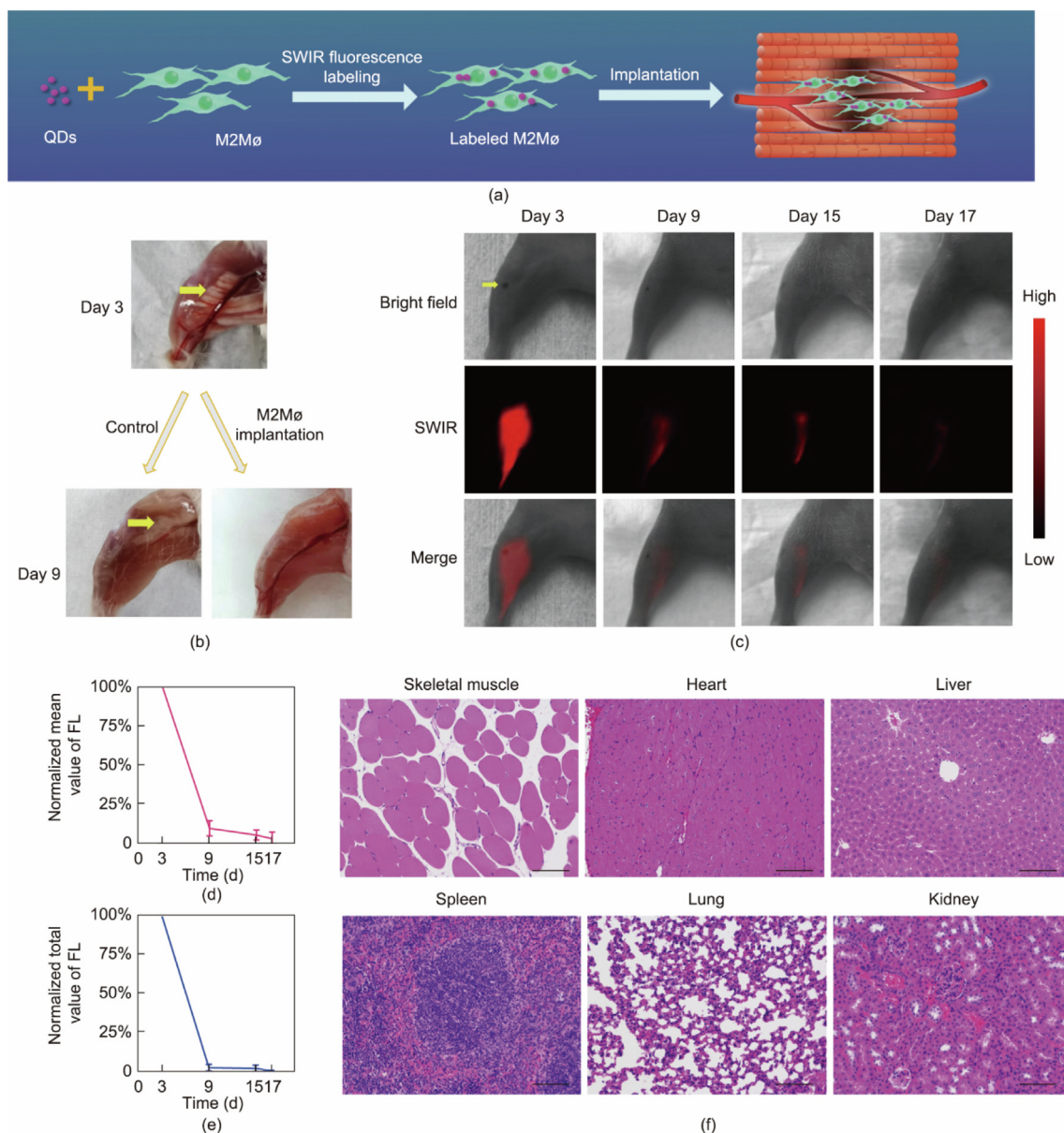

Fig. 3. M2Mø labeled with SWIR QDs implanted into injured skeletal muscle was traced via SWIR fluorescence imaging *in vivo*. (a) Schematic representation of labeling M2Mø with QDs, designed for tracking the fate of implanted M2Mø in injured skeletal muscle. (b) Gross morphology of injured skeletal muscle on day 9 post-injury with and without M2Mø implantation on day 3 post-injury (the arrow pointed to the necrotic area). (c) Injured skeletal muscle after implantation of M2Mø labeled with QDs under the bright field, the 808 nm SWIR laser (at exposure times of 80 ms), and merge on days 3, 9, 15, and 17 post-injury (the yellow arrow points to the injection site). Normalized (d) mean and (e) total value of FL of the fluorescence area on the injured skeletal muscle on days 3, 9, 15, and 17 post-injury. (f) H&E staining of different tissue and organs on day 17 post-injury (scale bar, 100 μm).

intramuscular injection of labeled M2Mø into the injured skeletal muscle on day 3 post-injury, while the intensity and area of fluorescence decreased significantly on day 9 post-injury, and the fluorescence only remained in a small area, which might be the severely injured area. Finally, the fluorescence of labeled M2Mø disappeared on day 17 post-injury. Quantitative analysis showed that the normalized mean and total value of FL had a significant decrease from day 3 to day 9 post-injury (90.2% ± 4.9%; 97.6% ± 2.2%) and a small decrease from day 9 to day 17 post-injury (6.7% ± 3.6%; 2.0% ± 1.8%) (Figs. 3(d) and (e)). This indicated that M2Mø persisted in the skeletal muscle for 14 days after implantation, and the main actuation time of M2Mø was within 6 days after implantation. Hematoxylin and eosin (H&E) staining of skeletal muscle and organs on day 17 post-injury showed that the accumulation of implanted M2Mø did not cause inflammation in the tissues and organs (Fig. 3(f)). This suggests that the implanted M2Mø could accumulate and remain in the injured areas for up to 14 days without causing tissue and organ inflammation.

3.3. Monitoring blood vessels by SWIR fluorescence imaging could be used as a sensitive indicator to evaluate degree of skeletal muscle regeneration

To investigate the outcome of M2Mø implantation in promoting skeletal muscle regeneration as a sensitive indicator to evaluate skeletal muscle, blood vessel evaluation in SWIR fluorescence imaging was introduced here to verify whether it was applicable to evaluate skeletal muscle regeneration in real time. As shown in Fig. 4(a), the normal skeletal muscle before the injury and the skeletal muscle of days 1 and 3 post-injury were compared, and no necrotic tissue was observed on day 1 post-injury by direct observation, while obvious necrotic tissue (necrotic area ratio = 0.64 ± 0.10) was observed on day 3 post-injury (Fig. 4(b) and (c)). The necrotic area was largest on day 3 post-injury (Fig. S1 in Appendix A). In SWIR fluorescence imaging, considering that FL gradually weakens with an increase in time after QDs injection, the stability of calculating the relative perfusion ratio with the
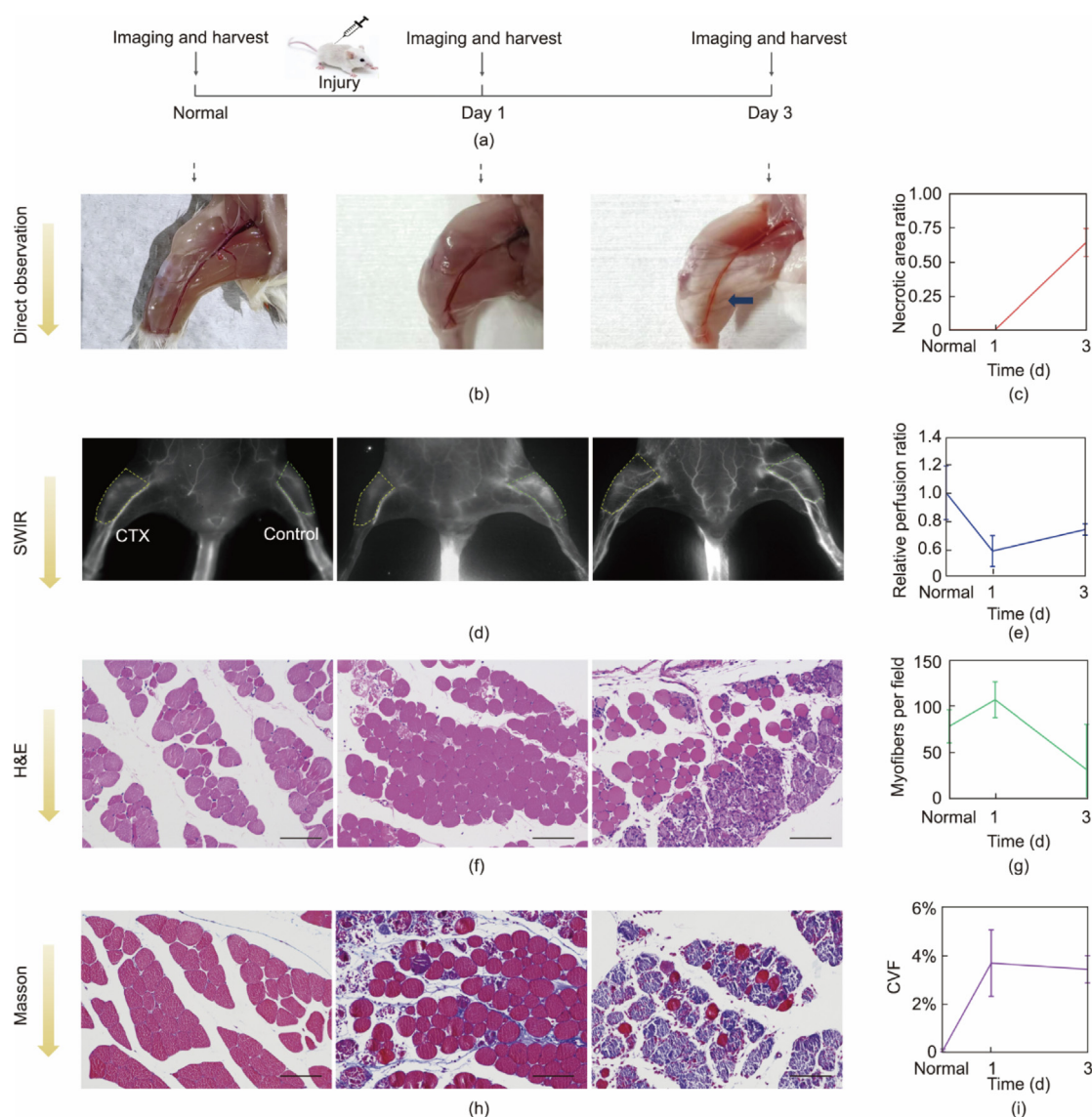
Fig. 4. (a) Normal skeletal muscle before injury and skeletal muscle on days 1 and 3 post-injury were imaged and harvested. (b) At direct observation, gross morphology of normal and injured skeletal muscle on days 1 and 3 post-injury (the arrow pointed to the necrotic area). (c) Necrotic area ratio directly observed was quantitatively assessed. (d) SWIR fluorescence imaging of normal skeletal muscle tissue and injured skeletal muscle on days 1 and 3 post-injury. (e) Relative perfusion ratio quantitatively assessed by SWIR fluorescence imaging. (f) H&E staining of normal skeletal muscle tissue and injured skeletal muscle on days 1 and 3 post-injury (scale bar, 100 μm). (g) Myofibers per field number (No.) assessed by H&E staining. (h) Masson staining of normal skeletal muscle tissue and injured skeletal muscle on days 1 and 3 post-injury (scale bar, 100 μm). (i) CVF assessed using Masson staining.

injection time was studied first. The relative perfusion ratio increased linearly with the increase in injection time within 35 s post-injection but remained stable at approximately 0.75 within 35 s to 4 min post-injection and was unaffected by the decrease in FL with injection time (Fig. S2 and Movie S1 in Appendix A). After confirming the stability of the relative perfusion rates as measured by SWIR fluorescence imaging, the skeletal muscle was imaged at the corresponding time points.

In contrast to the results of direct observation, the lowest relative perfusion ratio obtained by SWIR fluorescence imaging occurred on day 1 post-injury (Figs. 4(d) and (e)), indicating that the peak vascular injury occurred on day 1 post-injury (Fig. S3 in Appendix A). This was also confirmed by observation within 13 days post-injury. H&E staining of injured skeletal muscle confirmed the results of direct observation, and lower normal myofibers per field on day 3 post-injury compared to day 1 post-injury indicated that skeletal muscle injury was more severe on day 3 post-injury (Figs. 4(f) and (g)). Masson staining showed that the collagen volume fraction (CVF) on day 1 post-injury was the

highest among the time points analyzed, indicating that tissue repair began to be active on day 1 post-injury (Figs. 4(h) and (i)). In conclusion, vascular changes accompany the onset of repair and take precedence over the development of skeletal muscle changes. It could be seen that monitoring vascular changes through SWIR fluorescence imaging could be used as a sensitive indicator to monitor M2Mø involvement in skeletal muscle regeneration in real time.

3.4. In vivo and ex vivo results confirmed that M2Mø implantation in injured skeletal muscle could enhance angiogenesis and promote repair

After SWIR fluorescence imaging was proven to assess the quality of skeletal muscle regeneration, it was used to evaluate the efficacy of M2Mø implantation in injured skeletal muscle *in vivo*, and *ex vivo* testing was performed to validate its efficacy. Briefly, the gross morphology, SWIR fluorescence imaging of vessels, H&E staining, and Masson staining of injured skeletal muscle were
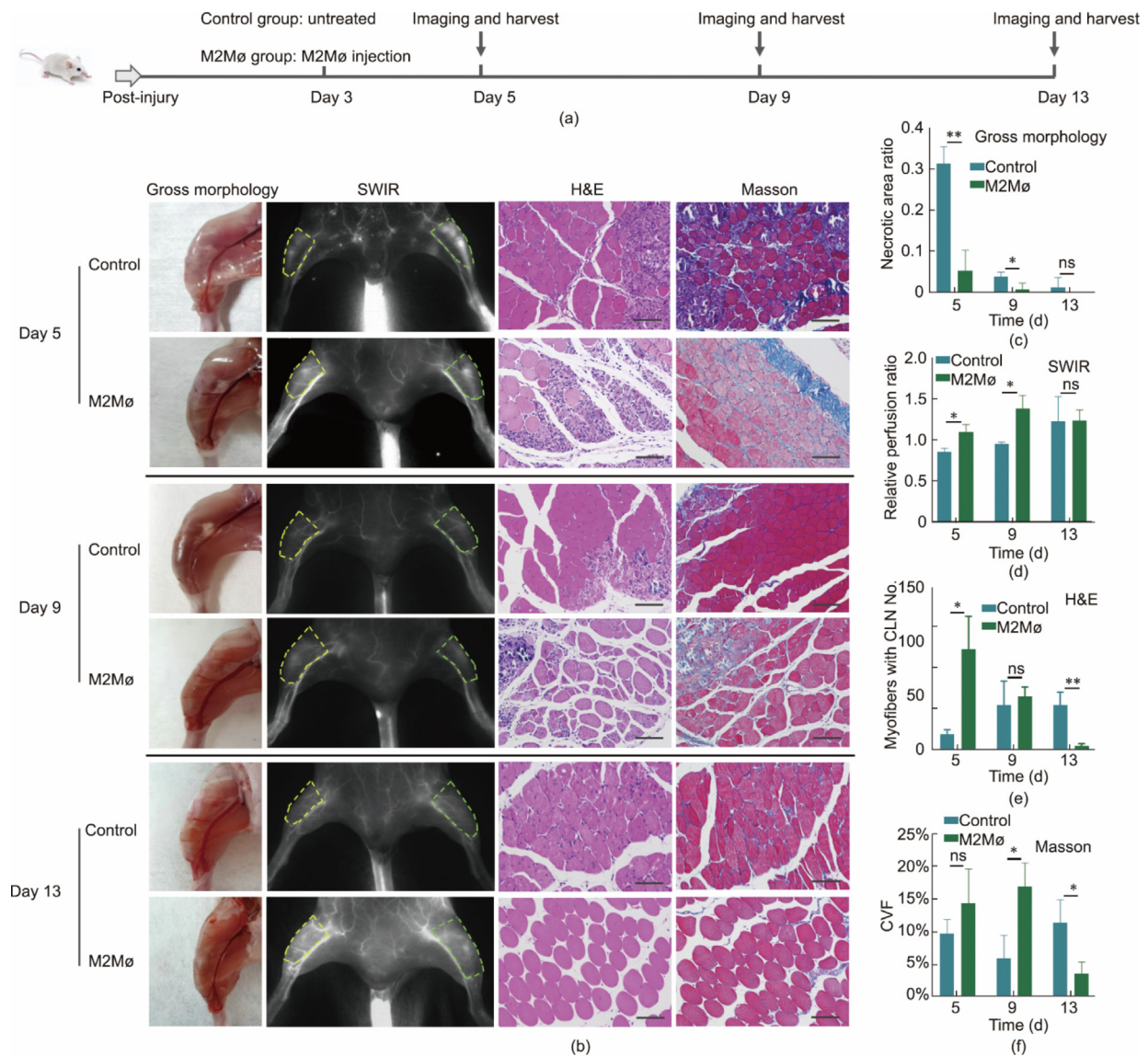

Fig. 5. *In vivo* and *ex vivo* comparison of M2Mø implantation group and control group. (a) After implantation of M2Mø into the injured skeletal muscle on day 3 post-injury, *in vivo* SWIR fluorescence imaging and *ex vivo* testing were performed on days 5, 9, and 13 post-injury. (b) Comparison of gross morphology, SWIR fluorescence imaging of vessels, H&E, and Masson staining between the control group and M2Mø implantation group on days 5, 9, and 13 post-injury (scale bar, 100 μm). (c) Necrotic area ratio, (d) relative perfusion ratio, (e) myofibers with CLN No., and (f) CVF of the control group and the M2Mø implantation group on days 5, 9, and 13 post-injury. ns: no significant difference.

compared between the M2Mø implantation group and the control group on days 5, 9, and 13 post-injury (Figs. 5(a) and (b)). According to the gross morphology, compared to the control group, the M2Mø implantation group had a significantly lower necrotic area ratio on days 5 (0.05 ± 0.05 vs 0.32 ± 0.04; $p < 0.01$) and 9 (0.01 ± 0.01 vs 0.04 ± 0.01; $p = 0.04$) post-injury, and comparable necrotic area ratio on day 13 post-injury (0 ± 0 vs 0.01 ± 0.02; $p = 0.37$) (Fig. 5(c)), indicating that the degree of repair of skeletal muscle injury significantly improved after M2Mø implantation. As for SWIR fluorescence imaging of vessels in skeletal muscle, relative perfusion ratio in the M2Mø implantation group were higher on day 5 (1.09 ± 0.09 vs 0.85 ± 0.05; $p = 0.01$) and day 9 (1.38 ± 0.16 vs 0.95 ± 0.03; $p = 0.01$) post-injury, whereas the relative perfusion ratio between the two groups had no significant difference on day 13 post-injury (1.23 ± 0.13 vs 1.23 ± 0.30; $p = 0.99$) (Fig. 5(d)). The richer blood flow perfusion in the M2Mø implantation group reflected greater angiogenesis on days 5 and 9 post-injury. As shown in Fig. 5(e), regenerating myofibers with centrally localized nuclei (CLN) numbers (No.) of the M2Mø implantation group was significantly more on day 5 post-injury (92.3 ± 30.1 vs 13.8 ± 4.0; $p = 0.01$), but there was no significant difference between the M2Mø implantation group and the control group on day 9 post-injury (48.4 ± 8.9 vs 40.7 ± 21.9; $p = 0.60$), and then became significantly less on day 13 post-injury (3.4 ± 1.8 vs 40.7 ± 11.8; $p < 0.01$). This gradual decrease indicated that the regeneration time of newborn myofibers was advanced by M2Mø implantation. Finally, from the results of Masson staining, CVF of the M2Mø implantation group showed no significant difference from that of the control group on day 5 post-injury (14.2 ± 5.2 vs 9.5 ± 2.2; $p = 0.22$), then significantly increased on day 9 post-injury (16.7 ± 3.6 vs 5.8 ± 3.5; $p = 0.02$) and significantly decreased on day 13 post-injury (3.4 ± 1.8 vs 11.2 ± 3.5; $p = 0.03$) (Fig. 5(f)). The relative perfusion ratio in SWIR fluorescence imaging significantly correlated with the necrotic area ratio in gross morphology and CVF in Masson staining (Figs. S4(a)–(c) in Appendix A), suggesting that the relative perfusion ratio was inextricably linked to the degree of repair of skeletal muscle injury and collagenation.

In conclusion, the M2Mø implantation could promote angiogenesis, increase collagenation, and thus advance the process of newborn myofibers regeneration and increase the degree of skeletal muscle regeneration.

3.5. IHC confirmed that implantation of M2Mø into injured skeletal muscle could enhance angiogenesis

IHC staining of CD163 and neovascularization biomarkers such as CD31, VWF, and α-SMA were used to quantitatively verify the number of M2Mø and neovascularization in the injured area of the skeletal muscle and confirm that implantation of M2Mø into injured skeletal muscle could enhance angiogenesis. Based on the CD163 immunohistochemical staining (Fig. 6(a)), the M2Mø implantation group had a higher mean of H-score values than those of the control group on days 5 (18.8 ± 7.5 vs 11.6 ± 2.0), 9 (12.6 ± 2.9 vs 9.7 ± 3.9), and 13 (16.2 ± 10.0 vs 12.5 ± 3.7) post-injury (Fig. 6(b)). Immunohistochemical staining of CD31 (Fig. 6(c)), the CD31 positive microvessel density (MVD) was comparable between the two groups on days 5 (220.8 ± 148.3 vs 198.4 ± 95.8; $p = 0.84$) and 9 post-injury (256.5 ± 87.2 vs 291.4 ± 43.1; $p = 0.57$); it only was significantly lower in the M2Mø implantation group on day 13 post-injury (294.0 ± 25.6 vs 690.3 ± 112.4; $p < 0.01$) (Fig. 6(d)). However, VWF positive H-scores were significantly higher in the M2Mø implantation group on days 5 (65.0 ± 12.1 vs 16.2 ± 21.4; $p = 0.03$) and 9 (80.4 ± 6.9 vs 3.5 ± 5.1; $p < 0.01$) post-injury (Figs. 6(e) and (f)). And according to the quantitative result of α-SMA IHC staining, the mean of α-SMA positive MVD in the M2Mø implantation group was higher on day 5 post-injury (116.0 ± 70.8 vs 30.6 ± 18.3; $p = 0.11$), was statistically significantly higher on day 9 post-injury (92.4 ± 32.4 vs 31.3 ± 9.0; $p = 0.03$), and had no significant difference with the control group on day 13 post-injury (172.3 ± 95.1 vs 202.4 ± 49.3; $p = 0.65$) (Figs. 6(g) and (h)). In conclusion, CD163, VWF, and α-SMA in the M2Mø implantation group were higher than those in the control group on days 5 and 9 post-injury, indicating that M2Mø implantation significantly increased neovascularization
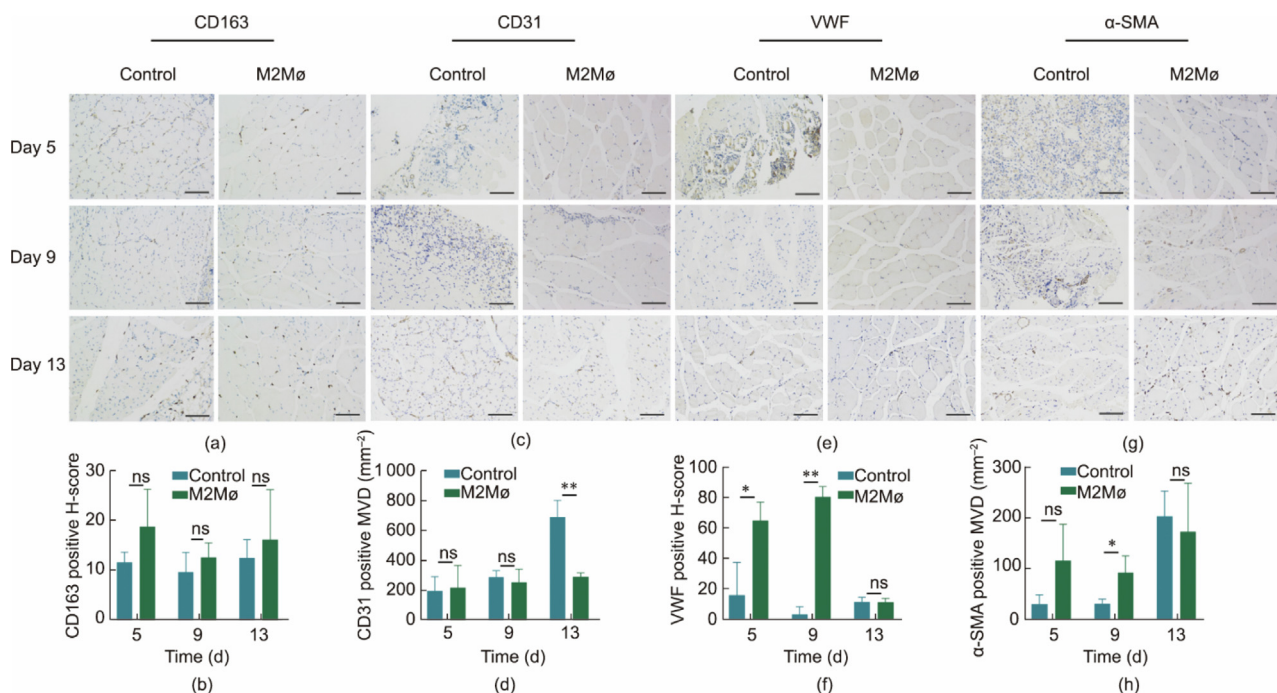
Fig. 6. Representative IHC images and quantitative analysis of (a, b) CD163, (c, d) CD31, (e, f) VWF, and (g, h) α-SMA of injured skeletal muscle in the two groups on days 5, 9, and 13 post-injury. Scale bar, 100 μm.

within nine days post-injury, and speed up the regeneration process.

3.6. Post-injury time and relative perfusion ratio were important indicators to evaluate degree of skeletal muscle regeneration

The degree of skeletal muscle regeneration, an important observational index in this study, was also the most important clinical monitoring result. Correlation analysis and multiple regression analysis of the observational factors of neovascularization and the degree of skeletal muscle regeneration were performed to explore the factors related to skeletal muscle regeneration and facilitate the assessment of the degree of regeneration. Among the IHC results of angiogenesis-related markers, only the VWF positive H-score was significantly correlated ($r = 0.51$, $p = 0.03$) with the relative perfusion growth rate (Fig. 7(a)), indicating that VWF might be an ideal option as an IHC angiogenesis-related marker for labeling neovascularization in skeletal muscles. And only α-SMA positive MVD was significantly correlated ($r = 0.45$, $p = 0.03$) with CD163 positive H-score (Figs. S4(d)–(f) in Appendix A). As shown in Fig. 7(b), post-injury time ($r = -0.46$, $p = 0.02$), relative perfusion ratio ($r = -0.44$, $p = 0.03$), and α-SMA positive MVD
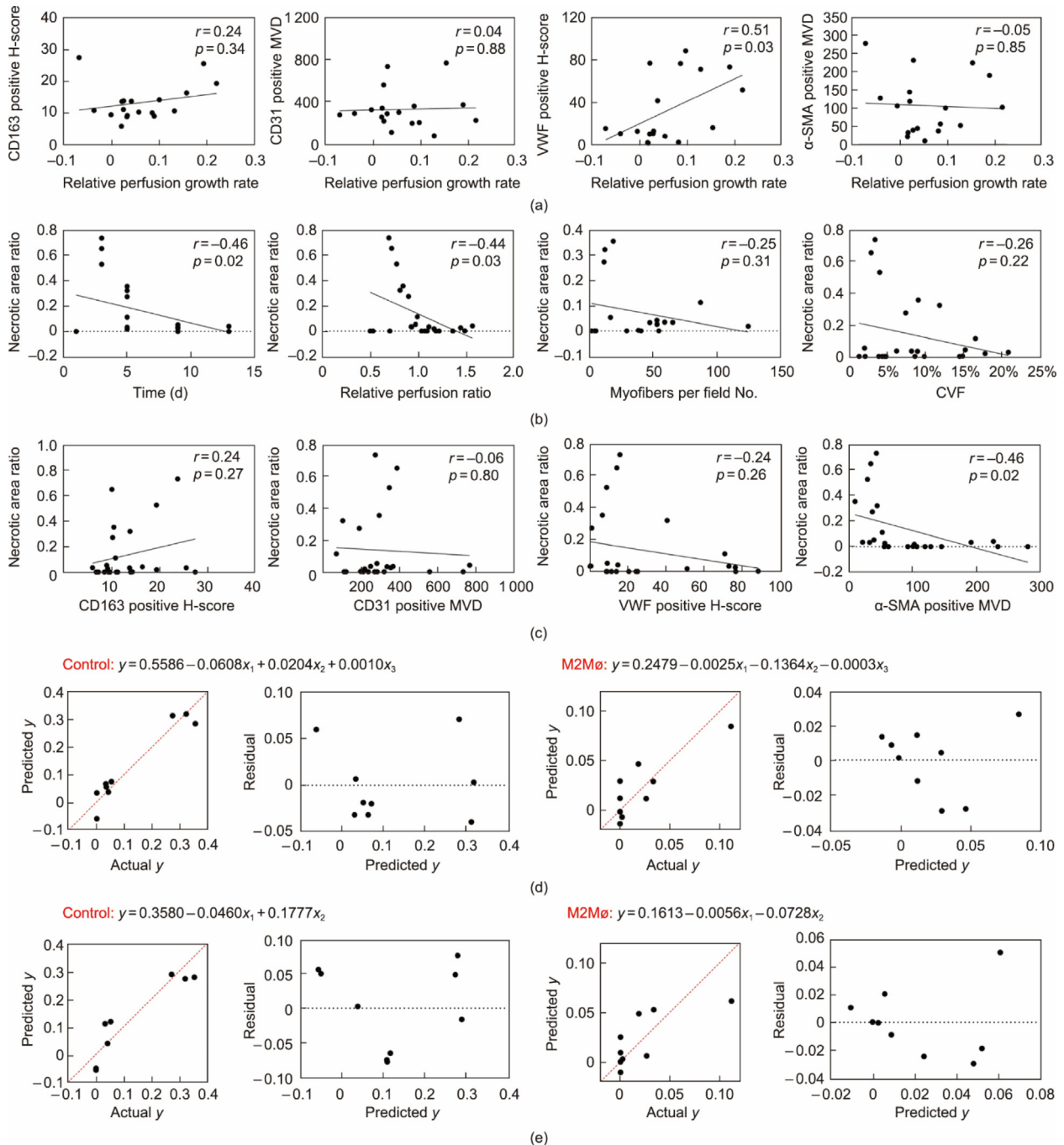

Fig. 7. (a) Correlation among CD163 positive H-score, CD31 positive MVD, VWF positive H-score, α-SMA positive MVD and relative perfusion growth rate. (b) Correlation among post-injury time, relative perfusion ratio, myofibers per field No., CVF, CD163 positive H-score, CD31 positive MVD, VWF positive H-score, α-SMA positive MVD and necrotic area ratio. (c) Multiple regression equation with post-injury time, relative perfusion ratio, and α-SMA positive MVD as independent variable and necrotic area ratio as dependent variable. (d) Multiple regression equation with post-injury time and relative perfusion ratio as independent variable and necrotic area ratio as dependent variable.

ARTICLE IN PRESS

M. Chen, Y. Chen, S. Feng et al.   Engineering xxx (xxxx) xxx

($r = -0.46$, $p = 0.02$) were significantly related to necrotic area ratio. Using these three indicators as independent variables (post-injury time—x_1, relative perfusion ratio—x_2, α-SMA positive MVD—x_3) for multiple linear regression analysis showed excellent fitting degree (the control group: $y = 0.5586 - 0.0608x_1 + 0.0204x_2 + 0.0010x_3$, $R^2 = 0.9240$; the M2Mϕ implantation group: $y = 0.2479 - 0.0025x_1 - 0.1364x_2 - 0.0003x_3$, $R^2 = 0.7143$) (Fig. 7(c)). Among the three independent variables, because α-SMA positive MVD was assessed *in vitro*, only post-injury time and relative perfusion ratio were used as independent variables for binary linear regression analysis to evaluate the degree of skeletal muscle regeneration by *in vivo* monitoring indicators. The results showed that although the fitting degree was slightly worse than that of the multiple linear regression analysis for three independent variables, the binary linear regression equation still had a good fitting degree (the control group: $y = 0.3580 - 0.0460x_1 + 0.1777x_2$, $R^2 = 0.8286$; the M2Mϕ implantation group: $y = 0.1613 - 0.0056x_1 - 0.0728x_2$, $R^2 = 0.5239$) (Fig. 7(d)). In summary, the post-injury time and relative perfusion ratio were important indicators to evaluate the degree of skeletal muscle regeneration. These two parameters could be used to assess the degree of skeletal muscle regeneration.

4. Discussion

In three days after injury before M2Mϕ implantation, the early stage of CTX-induced skeletal muscle injury was evaluated by direct observation, SWIR fluorescence imaging for vessels in skeletal muscle, H&E staining, and Masson staining. Among the four methods, SWIR fluorescence imaging of skeletal muscle vessels was the only indirect method for evaluating skeletal muscle quality. The severity of the vascular injury can be quantitatively assessed by calculating the relative perfusion ratio. SWIR fluorescence imaging showed that the relative perfusion ratio was the lowest on day 1 post-injury, indicating that vascular injury associated with skeletal muscle injury appeared rapidly and significantly and that monitoring vascular injury might indirectly monitor skeletal muscle injury on day 1 post-injury. Masson's staining supported the observation of vascular injury on SWIR fluorescence imaging. The fiber volume ratio on day 1 post-injury was higher than on day 3 post-injury, suggesting that collagenation was most active on day 1 post-injury. Nevertheless, both direct observation and H&E staining revealed that the severity of skeletal muscle necrosis was higher on day 3 than on day 1 post-injury. This suggests that although both vascular injury and skeletal muscle necrosis were caused by injury, the peak time of vascular injury occurred earlier than that of skeletal muscle necrosis. An obvious vascular injury could be detected by SWIR fluorescence imaging at the early stage of injury, proving that monitoring vascular injury could achieve an early diagnosis of skeletal muscle injury.

After M2Mϕ implantation, mean blood perfusion (relative perfusion ratio in SWIR fluorescence imaging), skeletal muscle quality (necrotic area ratio in direct observation), and regenerating myofibers (myofibers with CLN No. in H&E staining), and collagen (CVF in Masson staining) in the M2Mϕ implantation group were all higher than those in the control group, regardless of whether there were statistical differences on days 5 and 9 post-injury. This suggested that M2Mϕ significantly improved both angiogenesis and skeletal muscle regeneration quality during the first six days post-implantation. On day 13 post-injury, these indicators either did not differ significantly between the two groups or were reversed to significantly lower levels in the M2Mϕ implantation group. Moreover, these values were closer to normal skeletal muscles (Fig. 4), indicating that the skeletal muscle on day 10 post-implantation had been repaired to a state much closer to that of the normal skeletal muscle than the control group. Therefore,

M2Mϕ implantation promotes skeletal muscle regeneration, improves the quality of repair, and accelerates skeletal muscle regeneration.

Notably, the quantitative differences in CD31, one of the most commonly used and well-established markers [31], between the two groups contradicted those of VWF and α-SMA and were even higher in the control group than in the M2Mϕ implantation group on day 9 post-injury. Opposite levels of angiogenesis-related markers between the two groups have also been reported. Bösmüller et al. [32] compared microvessel density assessed by positive staining for CD31 and vascular endothelial growth factor receptor 2 (VEGFR-2) between intrahepatic cholangiocellular carcinoma and matched control tissue. Intrahepatic cholangiocellular carcinoma had significantly fewer VEGFR-2-positive microvessels (high power field (HPF): 15.4 (2.0–77.0)) than the matched control tissue (42.3 (4.6–109.0)), whereas microvessel density with CD31 was comparable between them (32.1 (5.3–78.0) vs 28.0 (5.3–57.0); $p = 0.89$). Different angiogenesis-related markers are expressed at different sites. For example, CD31 expresses on endothelial cells [31], α-SMA is found in pericytes that wrap around endothelial cells in the capillaries [33], and VWF is present in the subendothelial matrix [34]. Even for the two types of angiogenesis-related markers expressed on endothelial cells, the immunohistochemical expression of different antigens varied greatly. Figueiredo et al. [35] used the angiogenic-related markers CD31 and CD105 antibodies, expressed on endothelial cells, for double IHC labeling of polyether polyurethane-induced angiogenesis in mice and found that the number of blood vessels labeled by CD31 was significantly lower than that of CD105.

Moreover, the number of blood vessels stained with both markers was significantly lower than that of blood vessels counted in H&E staining. Figueiredo et al. [35] deemed these findings to show the limitation of double immunofluorescence of CD31 and CD105 in labeling neovessels in implants. This may also reflect the limitations and uncertainties of immunohistochemical staining. Furthermore, the status of CD31 as the most representative angiogenesis-related marker has been questioned, possibly because its expression levels may be affected by tissue and model types, even during angiogenesis. Van Amerongen et al. [36] found that CD31 was not, but collagen IV was, the best angiogenesis-related marker in the subcutaneous collagen type I disc model; and VWF, MECA-32, and endomucin antibodies frequently failed to stain newly formed blood vessels in this model. These results document the instability and limitations of *in vitro* assays, such as immunohistochemistry, and demonstrate the reliability of *in vivo* assays. Finally, we found that the variance in immunohistochemical statistics was large, which was also one of the main reasons for the lack of statistical difference between the two groups. However, the means of some marker expression levels seemed to be very different. In conclusion, the results of the immunohistochemical analysis of angiogenesis-related markers were affected by various factors and showed great uncertainty. This suggests that *in vivo* tests always precede selection when both *in vivo* and *in vitro* tests are available. Therefore, multiple markers are preferred to replace single-marker staining to comprehensively analyze the results and obtain more comprehensive information.

Finally, a regression equation was used for the necrotic area ratio based on the post-injury time and relative perfusion ratio in SWIR fluorescence imaging. As an intuitive result of skeletal muscle regeneration after injury, the necrotic area ratio was difficult to access directly because the skeletal muscle was covered under the skin and was observed by exposing the skin in this study. However, in clinical practice, invasive exposure cannot directly assess skeletal muscle injury; therefore, imaging methods such as magnetic resonance imaging (MRI) and computed tomography (CT) are often needed to evaluate [37,38]. Compared with the two latter methods,

SWIR fluorescence imaging vascular indirect assessment of skeletal muscle quality can avoid high prices, radiation, long appointments, and imaging; and facilitate doctors to realize real-time, rapid, and low-cost diagnosis in the consulting room. According to this equation, the necrotic area ratio can be calculated using the post-injury time and the measured relative perfusion ratio to determine the repair of the skeletal muscle. In conclusion, this study not only proved the effectiveness of M2Mø implantation in treating skeletal muscle injury but also used SWIR fluorescence imaging to evaluate the blood vessels in skeletal muscle to assist in assessing skeletal muscle regeneration quality. This paved the way for novel approaches to treating and evaluating skeletal muscle regeneration.

5. Conclusions

M2Mø implanted into the skeletal muscle on day 3 post-injury would accumulate in the injured area for up to 14 days. The implanted cells promote angiogenesis and accelerate the regeneration process to improve the degree of skeletal muscle regeneration. Time after injury, relative blood perfusion, and VWF-positive H-scores on IHC are important predictors of skeletal muscle regeneration. This study provides a novel strategy for *in vivo* monitoring and evaluating implanted M2Mø to improve skeletal muscle regeneration. It will pave the way for further research and application of M2Mø in the treatment of skeletal muscle diseases in the future, and future optimizations of devices and probes will help further extend biomedical applications.

Acknowledgments

Compliance with ethics guidelines

Appendix A. Supplementary material

Supplementary data to this article can be found online at https://doi.org/10.1016/j.eng.2023.05.010.

References

[1] Pedersen BK, Febbraio MA. Muscles, exercise and obesity: skeletal muscle as a secretory organ. Nat Rev Endocrinol 2012;8(8):457–65.

[2] Samandari M, Quint J, Rodríguez-Delarosa A, Sinha I, Pourquié O, Tamayol A. Bioinks and bioprinting strategies for skeletal muscle tissue engineering. Adv Mater 2022;34(12):e2105883.

[3] Dumont NA, Bentzinger CF, Sincennes MC, Rudnicki MA. Satellite cells and skeletal muscle regeneration. Compr Physiol 2015;5(3):1027–59.

[4] Pedersen BK. Muscle as a secretory organ. Compr Physiol 2013;3(3):1337–62.

[5] Palermi S, Massa B, Vecchiato M, Mazza F, De Blasiis P, Romano AM, et al. Indirect structural muscle injuries of lower limb: rehabilitation and therapeutic exercise. J Funct Morphol Kinesiol 2021;6(3):75.

[6] Järvinen TA, Järvinen TL, Kääriäinen M, Äärimaa V, Vaittinen S, Kalimo H, et al. Muscle injuries: optimising recovery. Best Pract Res Clin Rheumatol 2007;21(2):317–31.

[7] Haas GJ, Dunn AJ, Marcinczyk M, Talovic M, Schwartz M, Scheidt R, et al. Biomimetic sponges for regeneration of skeletal muscle following trauma. J Biomed Mater Res A 2019;107(1):92–103.

[8] Namsrai T, Parkinson A, Chalmers A, Lowe C, Cook M, Phillips C, et al. Diagnostic delay of myositis: an integrated systematic review. Orphanet J Rare Dis 2022;17(1):420.

[9] Zhang G, Tang M, Zhang X, Zhou S, Wu C, Zhao J, et al. Effects of conventional rehabilitative and aerobic training in patients with idiopathic inflammatory myopathy. Rheumatol Immunol Res 2022;3(1):23–30.

[10] Zhou D, King EH, Rothwell S, Krystufkova O, Notarnicola A, Coss S, et al. Low copy numbers of complement C4 and C4A deficiency are risk factors for myositis, its subgroups and autoantibodies. Ann Rheum Dis 2022;82(2):235–45.

[11] Porpiglia E, Mai T, Kraft P, Holbrook CA, de Morree A, Gonzalez VD, et al. Elevated CD47 is a hallmark of dysfunctional aged muscle stem cells that can be targeted to augment regeneration. Cell Stem Cell 2022;29(12):1653–8.

[12] Brett JO, Arjona M, Ikeda M, Quarta M, de Morrée A, Egner IM, et al. Exercise rejuvenates quiescent skeletal muscle stem cells in old mice through restoration of cyclin D1. Nat Metab 2020;2(4):307–17.

[13] Cruz-Jentoft AJ, Sayer AA. Sarcopenia. Lancet 2019;393(10191):2636–46.

[14] Ruehle MA, Li MA, Cheng A, Krishnan L, Willett NJ, Guldberg RE. Decorin-supplemented collagen hydrogels for the co-delivery of bone morphogenetic protein-2 and microvascular fragments to a composite bone-muscle injury model with impaired vascularization. Acta Biomater 2019;93:210–21.

[15] Baumann M, Gumpold C, Mueller-Felber W, Schoser B, Haberler C, Loescher WN, et al. Pattern of myogenesis and vascular repair in early and advanced lesions of juvenile dermatomyositis. Neuromuscul Disord 2018;28(12):973–85.

[16] Das A, Huang GX, Bonkowski MS, Longchamp A, Li C, Schultz MB, et al. Impairment of an endothelial NAD$^+$-H$_2$S signaling network is a reversible cause of vascular aging. Cell 2018;173(1):74–89.e20.

[17] Wynn TA, Chawla A, Pollard JW. Macrophage biology in development, homeostasis and disease. Nature 2013;496(7446):445–55.

[18] Shang M, Cappellesso F, Amorim R, Serneels J, Virga F, Eelen G, et al. Macrophage-derived glutamine boosts satellite cells and muscle regeneration. Nature 2020;587(7835):626–31.

[19] Ratnayake D, Nguyen PD, Rossello FJ, Wimmer VC, Tan JL, Galvis LA, et al. Macrophages provide a transient muscle stem cell niche via NAMPT secretion. Nature 2021;591(7849):281–7.

[20] Luo Z, Qi B, Sun Y, Chen Y, Lin J, Qin H, et al. Engineering bioactive M2 macrophage-polarized, anti-inflammatory, miRNA-based liposomes for functional muscle repair: from exosomal mechanisms to biomaterials. Small 2022;18(34):e2201957.

[21] Ma Q, Zhang N, You Y, Zhu J, Yu Z, Chen H, et al. CXCR4 blockade in macrophage promotes angiogenesis in ischemic hindlimb by modulating autophagy. J Mol Cell Cardiol 2022;169:57–70.

[22] Welsher K, Liu Z, Sherlock SP, Robinson JT, Chen Z, Daranciang D, et al. A route to brightly fluorescent carbon nanotubes for near-infrared imaging in mice. Nat Nanotechnol 2009;4(11):773–80.

[23] Smith AM, Mancini MC, Nie S. Bioimaging: second window for *in vivo* imaging. Nat Nanotechnol 2009;4(11):710–1.

[24] Yang Y, Chen J, Shang X, Feng Z, Chen C, Lu J, et al. Visualizing the fate of intra-articular injected mesenchymal stem cells in *vivo* in the second near-infrared window for the effective treatment of supraspinatus tendon tears. Adv Sci 2019;6(19):1901018.

[25] Chen M, Feng S, Yang Y, Li Y, Zhang J, Chen S, et al. Tracking the *in vivo* spatio–temporal patterns of neovascularization via NIR-II fluorescence imaging. Nano Res 2020;13(11):3123–9.

[26] Ying W, Cheruku PS, Bazer FW, Safe SH, Zhou B. Investigation of macrophage polarization using bone marrow derived macrophages. J Vis Exp 2013;76:50323.

[27] Kong Y, Chen J, Fang H, Heath G, Wo Y, Wang W, et al. Highly fluorescent ribonuclease-a-encapsulated lead sulfide quantum dots for ultrasensitive fluorescence *in vivo* imaging in the second near-infrared window. Chem Mater 2016;28(9):3041–50.

[28] Myers MJ, Shepherd DL, Durr AJ, Stanton DS, Mohamed JS, Hollander JM, et al. The role of SIRT1 in skeletal muscle function and repair of older mice. J Cachexia Sarcopenia Muscle 2019;10(4):929–49.

[29] Ma Z, Zhang M, Yue J, Alcazar C, Zhong Y, Doyle TC, et al. Near-infrared IIb fluorescence imaging of vascular regeneration with dynamic tissue perfusion measurement and high spatial resolution. Adv Funct Mater 2018;28(36):1803417.

[30] Paschalis A, Sheehan B, Riisnaes R, Rodrigues DN, Gurel B, Bertan C, et al. Prostate-specific membrane antigen heterogeneity and DNA repair defects in prostate cancer. Eur Urol 2019;76(4):469–78.

[31] Denize T, Farah S, Cimadamore A, Flaifel A, Walton E, Sticco-Ivins MA, et al. Biomarkers of angiogenesis and clinical outcomes to cabozantinib and

everolimus in patients with metastatic renal cell carcinoma from the phase III METEOR trial. Clin Cancer Res 2022;28(4):748–55.

[32] Bösmüller H, Pfefferle V, Bittar Z, Scheble V, Horger M, Sipos B, et al. Microvessel density and angiogenesis in primary hepatic malignancies: differential expression of CD31 and VEGFR-2 in hepatocellular carcinoma and intrahepatic cholangiocarcinoma. Pathol Res Pract 2018;214(8): 1136–41.

[33] Park IS, Mahapatra C, Park JS, Dashnyam K, Kim JW, Ahn JC, et al. Revascularization and limb salvage following critical limb ischemia by nanoceria-induced Ref-1/APE1-dependent angiogenesis. Biomaterials 2020;242:119919.

[34] Lagrange J, Worou ME, Michel JB, Raoul A, Didelot M, Muczynski V, et al. The VWF/LRP4/αVβ3-axis represents a novel pathway regulating proliferation of human vascular smooth muscle cells. Cardiovasc Res 2022;118(2):622–37.

[35] Figueiredo CC, Pereira NB, Pereira LX, Oliveira LAM, Campos PP, Andrade SP, et al. Double immunofluorescence labeling for CD31 and CD105 as a marker for polyether polyurethane-induced angiogenesis in mice. Histol Histopathol 2019;34(3):257–64.

[36] Van Amerongen MJ, Molema G, Plantinga J, Moorlag H, van Luyn MJ. Neovascularization and vascular markers in a foreign body reaction to subcutaneously implanted degradable biomaterial in mice. Angiogenesis 2002;5(3):173–80.

[37] He X, Zhang Y. Protective effect of amino acids on the muscle injury of aerobics athletes after endurance exercise based on CT images. J Healthc Eng 2022;2022:5961267.

[38] Kumaravel M, Bawa P, Murai N. Magnetic resonance imaging of muscle injury in elite American football players: predictors for return to play and performance. Eur J Radiol 2018;108:155–64.